Mineralogical characterization and speciation of sulfur, zinc and lead in pyrite cinder from Bergvik, Sweden

David Bendz [a,*], Charlotta Tiberg [a], Dan B. Kleja [a,b]

[a] Swedish Geotechnical Institute (SGI), SE-581 93, Linköping, Sweden
[b] Department of Soil and Environment, Swedish University of Agricultural Sciences (SLU), Box 7014, SE-750 07, Uppsala, Sweden

ARTICLE INFO

ABSTRACT

Roasting of sulfide ores to produce sulfuric acid began on an industrial scale in the middle 1800's and is still used extensively worldwide. The residual, pyrite cinders, have commonly been disposed in the environment where they pose a potential and serious threat to aquatic life. In this project, two profiles in a pyrite cinder deposit in Bergvik, Sweden, have been sampled and a comprehensive mineralogical characterization have been carried out. The objectives were to investigate the composition and morphology of pyrite cinder grains and the speciation of sulfur, Pb and Zn in the solid phase. Scanning electron microscopy showed pyrite cinder grains with a core of the ore minerals pyrite and sphalerite enclosed in layers of iron oxides/hydroxides (mainly hematite). XANES analysis, supported by X-ray diffraction analysis, SEM-EDS and bulk element analysis, showed that content of the residual sulfur in the cinder is mainly sulfides, 55–80%, predominately sphalerite. The remaining mass of sulfur is assumed to be adsorbed or precipitated as secondary sulfate minerals, predominantly associated with the grain surfaces. Calculated saturation indexes indicated barite, anglesite and perhaps aluminite. EXAFS spectroscopy indicated that about half of the Zn was bound to O and half was bound to S. LCF analysis of EXAFS spectra indicated that the main Zn species were sphalerite (40–50%) and franklinite (10–20%). The remaining Zn was associated with iron oxides/hydroxides and Zn minerals like hydrozincite or possibly zinc oxides. SEM-EDS analysis showed Pb precipitate located on both the surface of the grains and in the interior as inclusions. The analytical interpretation indicated anglesite.

1. Introduction

Roasting of sulfide ores to produce sulfuric acid began on an industrial scale in the middle 1800's and is still used extensively worldwide. The most common source of sulfur is recovery from natural gas and oil, but about 35% of the sulfur is obtained as sulfur dioxide from sulfide ore roasting (The Essential Chemical Industry - online, 2020). During sulfide ore roasting at about 900 °C, a series of physicochemical transformations occur. Sulfur dioxide is released and iron oxides, mainly hematite (Fe_2O_3) and magnetite (Fe_3O_4), are formed. As pyrite is the most abundant sulfide mineral, the residual is called pyrite cinder and contains mainly iron, oxygen, sulfur and trace elements such as Cd, Cu, Pb, Zn and As. In Sweden large amounts of pyrite cinders have historically been disposed in the environment, commonly adjacent to surface water where they pose a potential and serious threat to aquatic life. The disposal sites are mainly located in the surroundings of pulp mill plants, where the sulfuric acid was used in the process of producing wood pulp.

Under the influence of exposure to atmosphere and water, remaining sulfides in the pyrite cinder can be oxidized after disposal. Acid leachate may occur and mobilize trace metals and arsenic (Jambor, 2003; Lin and Qvarfort, 1996; Yang et al., 2009).

The roasting of pyrite grains proceeds according to a shrinking core model, leaving a partially reacted grain with a core of unreacted pyrite and a shell or rim of mainly hematite or magnetite and sulfates as minor reactions products (Eneroth and Bender Koch, 2003; Hu et al., 2006). At higher temperatures pyrrhotite may also form as an intermediate product (Hu et al., 2006). Volatile elements such as Pb, originally typically present as galena, will partly vaporize and condensate downstream at temperatures lower than 600 °C (Díaz-Somoano et al., 2006). Theoretical work (Díaz-Somoano et al., 2006) and experimental studies (Folgueras et al., 2003; Liu et al., 2017; Miller et al., 2002) show that the presence of sulfur favours the forming of condensed sulfate phases, such as anglesite ($PbSO_4$), on grain surfaces. Such phenomena have also been reported in experimental work by (Sandell et al., 1996) who investigated

* Corresponding author.
E-mail addresses: david.bendz@sgi.se (D. Bendz), charlotta.tiberg@sgi.se (C. Tiberg), dan.berggren.kleja@sgi.se (D.B. Kleja).

Pb-rich phases in municipal solid waste incineration fly ash. Zinc, typically present as sphalerite (ZnS), has been shown to oxidize with only limited vaporization (Yang et al., 2009) and form zincite (ZnO) and franklinite ($ZnFe_2O_4$) (see Balarini et al., 2008 and references therein). Due to an incomplete roasting process, the resulting pyrite cinder may also contain unreacted sulfide mineral, such as pyrite, pyrrhotite and sphalerite (Lin and Qvarfort, 1996; Oliveira et al., 2012; Yang et al., 2009). Sphalerite can be oxidized by either dissolved molecular oxygen or ferric iron, but only the latter pathway produces acidity. However, if the ferric iron has been produced by oxidation of ferrous iron in the system there is no net effect on acidity. Sphalerite is therefore commonly considered to be a non-acid producing mineral. (Dold, 2010; Heidel et al., 2011; Moncur et al., 2009).

After disposal in the field and as the sulfide oxidation progress, the surfaces may become progressively enriched with secondary minerals, mainly iron (hydr)oxides, jarosite ($KFe_3(OH)_6(SO_4)_2$), iron sulfates and elemental sulfur (Jambor, 2003; Lapakko, 2002; Lin and Qvarfort, 1996; Nordström, 1982). During oxidation, hydrolysis and neutralization, hydroxysulfates of iron and aluminium may precipitate (Bigham and Nordstrom, 2000; Sánchez España et al., 2006).

Basic information of the mineralogy and the speciation of trace elements in the matrix is needed to assess the short- and long-term risks associated with pyrite cinder deposits, and for development of suitable remediation and management techniques. A vast amount of studies on oxidation of sulfide minerals is available due to the environmental problems associated with acid production by mine wastes (tailings or waste rock), see classical work by (Caruccio, 1968; Garrels and Thompson, 1960; McKibben and Barnes, 1986; Singer and Stumm, 1970; Williamson and Rimstidt, 1994). However, chemical and mineralogical characterization of pyrite cinder has only been carried out in a limited number of studies (Lin and Qvarfort, 1996; Oliveira et al., 2012; Pérez-López et al., 2009; Tiberg et al., 2017; Yang et al., 2009).

In this project, two profiles in a 60-year-old pyrite cinder deposit in Bergvik, Sweden, have been sampled. A comprehensive mineralogical characterization and speciation of sulfur, Pb and Zn have been carried out. The same deposit was studied in Tiberg et al. (2017), and hematite was then identified as the dominating iron mineral. Poorly crystalline iron (hydr)oxides, subsequent precipitated after oxidation of the unreacted sulfides in the field, were present in smaller quantities. By a combination of batch experiments, selective extractions, and geochemical modelling it was proposed that adsorption to iron oxides/hydroxides was an important retention mechanism for Cd, Cu, Pb and Zn. In addition, Zn minerals; ZnO and/or $Zn(OH)_2$, seemed to control concentrations of Zn in solution at high pH (pH > 6–7). It is well known that many metals form strong inner-sphere complexes on iron (hydr)oxide surfaces (Peacock and Sherman, 2004; Spadini et al., 1994; Trivedi et al., 2003).

Here, our objectives were to investigate the composition and morphology of grains and the speciation of sulfur, Pb and Zn in the Bergvik cinder. A combination of complementary techniques was used to analyze the solid phase. Scanning electron microscopy and energy-dispersive X-ray spectroscopy were used to study morphology and obtain spatially resolved information on the composition of the cinder grains. X-ray adsorption spectroscopy, X-ray diffraction analysis, and bulk element analysis provided information on main minerals and speciation in the solid phase.

2. Materials and methods

2.1. Pyrite cinder sampling

The sampling was carried out November 27th, 2013 at the former pulp mill plant in Bergvik outside Söderhamn in Sweden where about 110 000 m^3 pyrite cinder has been landfilled along the shore of Lake Smalsjön until the middle of the 1960's. Aerial photos show that the sampling took place in an area that was landfilled before 1951

Table 1
Samples of pyrite cinder samples collected in Bergvik.

Sample Pit, level	Depth fr. surface (m)	Ground water level (m)[a]
Cinder 1a	1.4	2.7
Cinder 1b	1.9	2.7
Cinder 1c	2.8	2.7
Cinder 2a	0.2	2.1
Cinder 2b	1.4	2.1
Cinder 2c	2.2	2.1

[a] Depth from surface.

(Figure S1). The coordinates of the sampling points are given in table S1. The cinder deposit was several meters thick above the ground water surface. In some areas it was covered with about 0.1–1 m of soil. The vertical profiles seemed to be rather homogenous and no mixing with other materials was observed. Samples were collected from two sampling pits (pits 1 and 2) at three levels; *level a*, close to the ground surface, *level b*, between the ground surface and the ground water table and *level c* just at the ground water surface (Table 1). A total of six large samples (approx. 5 kg each) were brought to the laboratory. To prevent oxidation of sulfides before the start of the experiments, the samples were collected in double non-diffusive plastic bags. The samples were put in air-tight plastic containers, flushed with N_2 gas before sealing and stored in the laboratory at 8 °C until used in the experiments.

2.2. Total content

Total (pseudo-total) concentrations of metals in solid samples were analyzed with ICP-SFMS after acid digestion with HNO_3/HCl/HF mixture (Pb and Zn) according to ASTM D3683 or melting with $LiBO_2$ and subsequent digestion with HNO_3 (Fe, Al) according to ASTM D3682.

Bulk element analysis of total sulfur, sulfide content and total carbon were conducted by infrared spectroscopy (Leco analyzer). While a stream of oxygen was allowed to pass through a prepared sample (0.05–0.6g), it was heated in an induction furnace to approximately 1350 °C. Sulfur dioxide and carbon dioxide released from the sample were measured by an infrared detection system and the total sulfur and total carbon result were provided. The sulfide content was analyzed by preparing the samples by selectively leaching in warm sodium carbonate solution to convert the metal sulfate into insoluble carbonates and soluble sulfate. The resulting residue was removed by filtration and the sulfide residue washed free of carbonate solution and analyzed.

Total organic carbon (TOC) and total inorganic carbon (TIC) concentrations in solid samples where determined according to ISO 10694 and EN 13137.

The bulk analysis was carried by ALS Scandinavia AB, accredited pursuant to ISO 17025.

2.3. Saturation indexes

Visual Minteq 3.1 was used to calculate saturation indexes (SI) of a range of minerals at the eigen pH of the pyrite cinder. The calculations were based on leaching data from batch experiments with four samples (Cinders 1a, 1c, 2a, and 2c) at L/S 10 after allowing to equilibrate for 5 days (Tiberg et al., 2017). The pH were in the range of pH 6.5–7, which is rather high for pyrite cinder (Tiberg et al., 2017). Pyrite cinder might have a pH as low as 2.3 (Lin and Qvarfort, 1996), but pyrite cinder with a neutral pH has also been reported in other studies (Vamerali et al., 2009). Franklinite was not present in the standard set of minerals in the Visual Minteq database but was added as it has been identified in smelter contaminated materials (Roberts et al., 2002).

Table 2

Samples for EXAFS and XANES measurement and reference spectra used in evaluation.

Sample	Measurements	Preparation/reference
Cinder 1a	Zn, S	Grinding in ball mill or homogenization in mortar.
Cinder 1c	Zn, S	Grinding in ball mill
Cinder 2a	Zn, S	Grinding in ball mill
Cinder 2c	Zn, S	Grinding in ball mill
Zn adsorbed on ferrihydrite	Zn	30 μmol L^{-1} Zn equilibrated for 24 h with 0.3 mmol L^{-1} ferrihydrite prepared according to the procedure of Schwertmann and Cornell (Schwertmann and Cornell, 2000).
ZnS	Zn	Zigma-Aldrich (99% purity)
ZnFe$_2$O$_4$	Zn	Steenari and Norén (2008)
ZnAl$_2$O$_4$	Zn	Steenari and Norén (2008)
ZnO	Zn	Medas et al. (2014)
ZnCO$_3$	Zn	Medas et al. (2014)
Hydrozincite	Zn	Medas et al. (2014)
Hemimorphite	Zn	Medas et al. (2014)
Willemite	Zn	Medas et al. (2014)
Pyrite	S	Sandström et al. (2005)
Sphalerite	S	ESRF (2019)
Troilite	S	Almkvist et al. (2010)
NaSO$_4$, 30 mmol L^{-1}	S	

2.4. X-ray diffraction, Scanning Electron Microscopy and energy-dispersive X-ray spectroscopy

X-ray powder diffraction (XRD) was used to identify crystalline minerals in the samples. XRD patterns were collected with a Panalytical X'pert powder diffractometer equipped with an X'celerator silicon-strip detector. Scan range: 5–70° (2θ), step-size 0.017°, using a sample spinner with the sample mounted on a background-free holder. Radiation: CuKα (1.54059 Å).

The software used was HighScore Plus 3.0 (Panalytical) and the database where the match units came from was ICSD. Scanning Electron Microscopy (Hitachi S–3400N) and Energy-dispersive X-ray spectroscopy (Oxford instruments Inca X-sight) was performed at the laboratory of the Department of Geology, Lund University, Sweden, to investigate the morphology and elemental composition of the pyrite cinder grains from sample Cinder 1a and Cinder 2a. To investigate the interior of the grains the samples were prepared to show a cross section. Epoxy resin was mixed with hardener, poured over the sample and allowed to harden. The sample was ground and polished to reveal the internal structure and chemical composition.

2.5. XAS measurements

Pyrite cinder samples were ground in a ball mill before analysis to homogenize the samples and reduce grain size. Additionally, spectra were collected from a few samples after grinding by hand in a mortar to ensure that the ball mill grinding did not affect the speciation of the sample. The samples were packed in aluminum frames and sealed with tape. Standard spectra were used to aid the interpretation of the XAS

Table 3

Average, min and max of the total content of Pb, Zn, Fe, S, Sulfides, TC and TIC. Values are based on all six samples, in duplicate.

Element	Average	Min	Max
Pb (mg kg^{-1} dw)	8470	6360	10 600
Zn (mg kg^{-1} dw)	29 100	13 200	37 900
Fe (wt%)	44	41	46
Stot (wt%)	1.90	1.38	2.47
Sulfides (wt%)	1.38	0.96	2.09
TC (wt%)	0.37	0.20	0.79
TIC (wt%)	0.15	0.05	0.22

data. Some standard spectra were collected within the project and some were published elsewhere, see Table 2. Spectra for lead could not be collected with good enough quality at the present conditions and lead concentrations. Lead has a wide Pb–O bond-range distribution and low symmetry (Persson et al., 2011), which makes it difficult to obtain good lead spectra.

XAS spectra of samples Cinder 1a, Cinder 1c, Cinder 2a and Cinder 2c were collected at the wiggler beam line I811, MAX-Lab, Lund, Sweden. Beam line I811 operated at 1.5 GeV with a maximum ring current of 400 mA and electrons were refilled twice a day. The end-station was equipped with a Si [111] double crystal monochromator. The measurements were performed in fluorescence mode using a PIPS detector. EXAFS spectra were collected at the Zn K-edge at 9659 eV with a Cu filter and a detuning of −20%. Samples were packed in an aluminum frame sealed with tape. A Zn foil was used for reference. Sulfur XANES spectra were collected at the sulfur K-edge 2472 eV with detuning 70%. Sodium sulfate was used as a reference and an extra mirror was put in to achieve the right energy. Samples were mounted in as thin layers on sulfur-free tape and ion-chambers had a slight over-pressure of helium to avoid absorbance of the beam by air during measurements.

All EXAFS spectra were treated in the Athena software (version 0.9.20) (Ravel and Newville, 2005). The background was removed using the AUTOBAK algorithm incorporated in Athena, with a *k*-weight of 2 or 3 and with the Rbkg parameter set to 1. Wavelet transform (WT) analysis of EXAFS spectra (Funke et al., 2005) was performed to differentiate between light (e.g. C, O) and heavy elements (back-scatterers) at 2.5–4.5 Å from the measured element. This qualitative analysis of backscattering contributions from higher shell atoms was performed for Zn spectra and models. The Morlet WT incorporated in the Igor Pro script (Chukalina, 2010) was used with the parameter combination $\kappa = 7$ and $\sigma = 1$ and a range of $R + \Delta R$ from 2 to 4 Å (corresponding to interatomic distances of about 2.5–4.5 Å). The *k*-ranges in WT analysis were the same as in the EXAFS fitting procedure.

Final data treatment of the Zn EXAFS spectra was performed with the Artemis software (version 0.0.012) (Ravel and Newville, 2005). Theoretical scattering paths were calculated with FEFF6 (Zabinsky et al., 1995). During the fitting procedure, the amplitude reduction factor (S_0^2) was set based on fitting of this parameter for the first coordination shell. For Zn spectra, the fitting procedure was performed on the Fourier transform real part between 1 and 4.5 Å using a Hanning window (dk value = 1) and optimizing over k-weights of 1, 2 and 3. Several combinations of scattering paths including Zn–O/S, Zn···Fe/Zn/S distances and multiple scattering (MS) paths were tested in the fitting procedure before deciding what paths to use. The first shell was fit with the Debye-Waller factors (σ^2) set at 0.006 to investigate the coordination numbers (CN) of the Zn–O and Zn–S paths. The parameters of the first shell were then fixed during fitting of higher shells. The coordination numbers were fixed for the higher shells and chosen to give reasonable values of σ^2. For multiple scattering paths (triangular paths for ZnO$_4$ and ZnS$_4$ tetrahedra) CN was defined to be three times CN for the single scattering path and σ^2 was set to of twice the σ^2 for the single scattering path. Refined models were evaluated by means of goodness-of-fit (as evidenced by the R factor in Artemis) and qualitative comparison of WT plots of the model spectra with WT plots of the EXAFS spectra. WT of the model spectra were made with the same WT-parameters and k-ranges as for measured spectra.

Linear combination fitting (LCF) was performed in Athena on k^3-weighted χ data from $k = 2.5$–10 Å^{-1}. All reference spectra listed in 0 were tried in the fits. All possible combinations between four or less of the reference spectra were evaluated. No energy shifts were allowed. The fits were run with standards having a weight between 0 and 1 constraining the sum to 1.

Sulfur XANES spectra were evaluated by comparison of peak positions with reference spectra of sulfur species with different oxidation numbers (Almkvist et al., 2010; Debret et al., 2017; ESRF, 2019; Sandström et al., 2005).

Table 4
Minerals identified by X-ray diffraction analysis.

Sample	Identified minerals	Uncertain minerals
Cinder 1a	Hematite, Quartz	Talc, Magnetite
Cinder 1b	Hematite, Sphalerite, Quartz	
Cinder 1c	Hematite, Quartz	
Cinder 2a	Hematite, Quartz	Sphalerite,
Cinder 2b	Hematite, Quartz, Sphalerite,	Chlorite
Cinder 2c	Hematite, Quartz, Sphalerite,	Talc, Amphibole

3. Results and discussion

3.1. Total content, extractable fraction and mineralogy by X-ray diffraction

The total content of selected heavy metals in the pyrite cinder is given in Table 3.

The bulk element analysis showed that 55–80% of the residual sulfur in the samples was sulfide. The average total content of sulfur and sulfide was 1.90% (593 mmol/kg) and 1.38% (431 mmol/kg), respectively.

The total concentrations of Zn and Pb were high in the pyrite cinder; especially Zn, ranging between 1.3 and 3.8% by weight (Table 3). About 30–50% of Zn and most of Pb (60–100%) could be extracted with EDTA (Tiberg et al., 2017). EDTA form strong complexes with divalent cations and thus scavenge cations from surfaces of both (hydr)oxides and organic matter (Sahuquillo et al., 2003). Dissolution of some mineral precipitates during extraction cannot be excluded as EDTA is a weak acid. This indicates that a large part of Pb was adsorbed to mineral surfaces or bound in minerals dissolved by EDTA while a considerable part of Zn was strongly bound in minerals and/or occluded in iron (hydr) oxide precipitates, resulting in either slow reaction kinetics, physical constraints to equilibrate with the solution or a combination of both (See also section 3.4.).

X-ray diffraction identified hematite and quartz (SiO₂) in all samples, and sphalerite in several samples. Some other minerals were also indicated but their identification was uncertain (Table 4).

3.2. Morphology and elemental composition of the grain surfaces

The typical morphology of two types of pyrite cinder grains, size 0.1 mm–0.3 mm, commonly found in the samples is shown in Fig. 1.

The first grain (Fig. 1, image *A*) is iron oxides/hydroxides (mainly hematite), possible covering a core of unreacted ore mineral. The other grain (Fig. 1, image *B*) is a mixture of iron (hydr)oxides, amphibole (needle-like form pointing down to the right, denoted *1* in the image *B*) and quartz (crystal pointing straight down, denoted *2* in the image *B*). Low concentrations of Pb and As scattered over the surfaces were detected. At the surface, small Pb-bearing precipitates are white/light
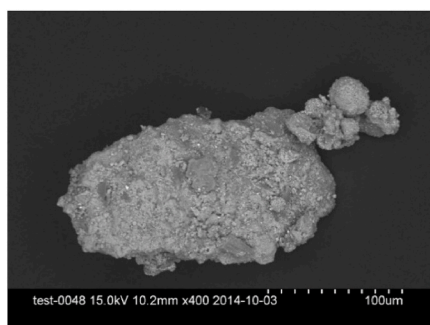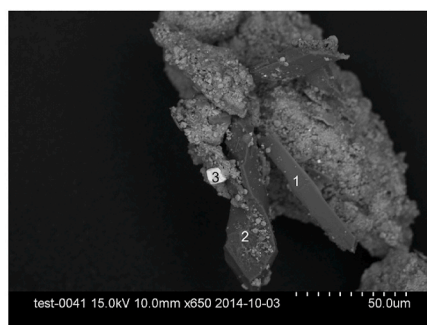
grey spots. Such precipitates were found on most of the grains. A larger white/light grey precipitate can be seen on the surface (denoted *3* in image *B*). The EDS-spectra of the precipitate showed mainly Fe, O, S, Pb and small amounts of As (Fig. 7).

3.3. Speciation of sulfur

3.3.1. XANES analysis of bulk composition

The positions of peaks in sulfur K-edge XANES spectra are sensitive to the sulfur oxidation state. The cinder spectra are shown in Fig. 2 together with standard spectra; sphalerite at 2473.8 eV, pyrite at 2472.1 eV, troilite 2470.8 eV (ESRF, 2019)) and sulfate S (+VI) at 2482.5 eV (Almkvist et al., 2010). The sulfur XANES spectra from the pyrite samples all have the same characteristic peaks, one at about 2482.5 eV, clearly present in all samples, and one at about 2472 eV, which is obvious in some samples but very small in some samples. The sulfate (S (+IV)) peak at about 2482.5 eV corresponds to sulfate minerals and adsorbed sulfate and the broader peak at about 2473–2474 eV to sulfide minerals (S (–II), S (–I)), where sphalerite is the most evident. Elemental sulfur that has peak at 2473 eV may also contribute to the broader peak.

Due to self-adsorption in the samples it was not possible to quantify the contribution from different forms of sulfur in the XANES analysis (Almkvist et al., 2010). In addition, the sample preparation procedure selected for the finest grains may lead to an overestimation of the

Fig. 2. Sulfur k-edge XANES. Representative cinder spectra and standards for sulfate and sphalerite. [Print in color].

A   B

Fig. 1. SEM images of (A and B) of two typical morphologies of pyrite cinder grains. The grains are mainly composed of iron oxides/hydroxides. Amphibole (1), quartz (2) and a white/light grey Pb-bearing precipitate (3) are shown in image B.
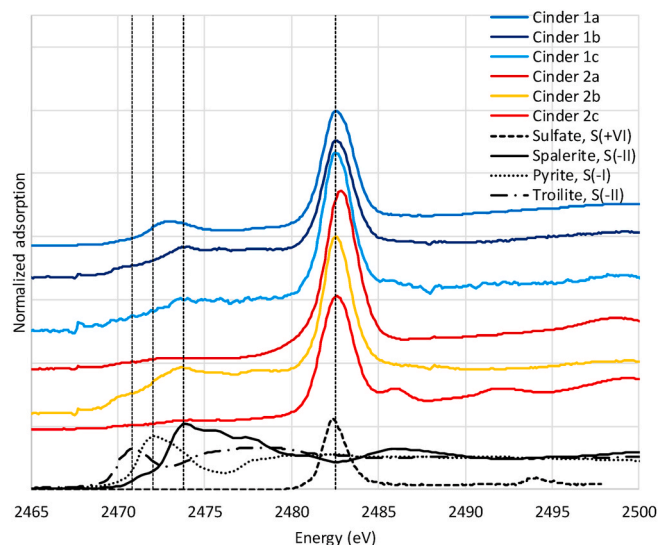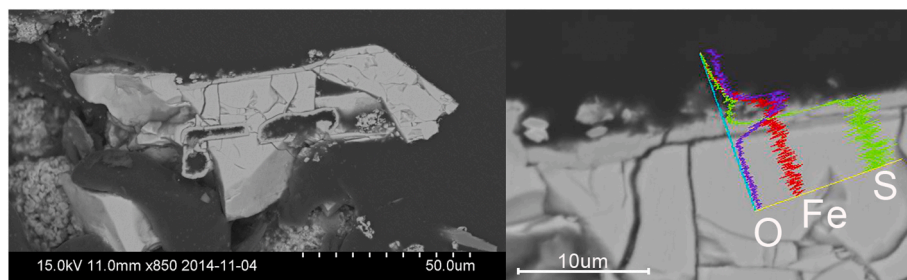
Fig. 3. SEM images of a cross-section of a grain with a grey shell of hematite and iron (hydr)oxides and the unreacted ore mineral as light grey/white. The result from an EDS line scan is shown in the magnified image at the right (green: sulfur, red: iron, purple: oxygen). [Print in color].

proportion of S (+VI) (adsorbed or surfaces precipitates), compared to sulfides in the bulk cinder. Note that the results from the bulk element analysis showed that sulfide fraction dominated (Table 3).

3.3.2. SEM-EDS analysis of the grain cross section

Fig. 3 shows a cross-section of a grain with a grey shell of iron (hydr) oxides. The sulfide mineral is relatively denser than iron (hydr)oxides and appears as light grey colored. The result from an EDS line scan is shown in the magnified image at the right (green: sulfur, red: iron, purple: oxygen). This illustrates an expected elemental sequence resulting from a partial oxidation of pyrite grain (Eneroth and Bender Koch, 2003; Hu et al., 2006).

The EDS line scan (Fig. 3) reflects the composition of the sulfide ore, an oxidized shell of iron (hydr)oxides and secondary sulfate bearing minerals or adsorption, indicated by a small peak of sulfur, at the surface of the grain. The dominating secondary sulfur mineral typically found in field samples of weathered pyrite in mining waste repositories is iron sulfate, either divalent or trivalent. At lower pH, schwertmannite

($Fe_8O_8(OH)_6(SO_4) \cdot nH_2O$ or $Fe^{3+}_{16}O_{16}(OH,SO_4)_{12-13} \cdot 10-12H_2O$) and jarosite ($KFe_3^{+3}(OH)_6(SO_4)_2$) are the dominating sulfate minerals (Bigham and Nordstrom, 2000; Jambor, 2003). In this study, neither schwertmannite nor jarosite were indicated by comparing the analyzed Fe-EXAFS spectra to schwertmannite and jarosite spectra given in (Miot et al., 2016) and (Savage et al., 2000), respectively. This can be explained by the neutral pH of the pyrite cinder in this study.

Data from the pH-dependent batch test (EN14429) shows that pH is the main state parameter governing the leachability of sulfur (see Figure S2). The difference of the solubility of sulfur, over the pH-range considered here, is about 10–40 mmol/kg, which is less than 10% of the total content of sulfur. This may be explained by pH dependent adsorption and precipitation of sulfate minerals. Experimental studies report that only negligible amounts of SO_4^{-2} are adsorbed above pH 6.5 (CURTIN and SYERS, 1990; GUADALIX and PARDO, 1991). The calculation of the saturation indexes indicated aluminite ($Al_4(OH)_{10}SO_4$), barite ($BaSO_4$) and anglesite as possible sulfate secondary minerals. Anglesite and barite were close to saturation at eigen pH and aluminite
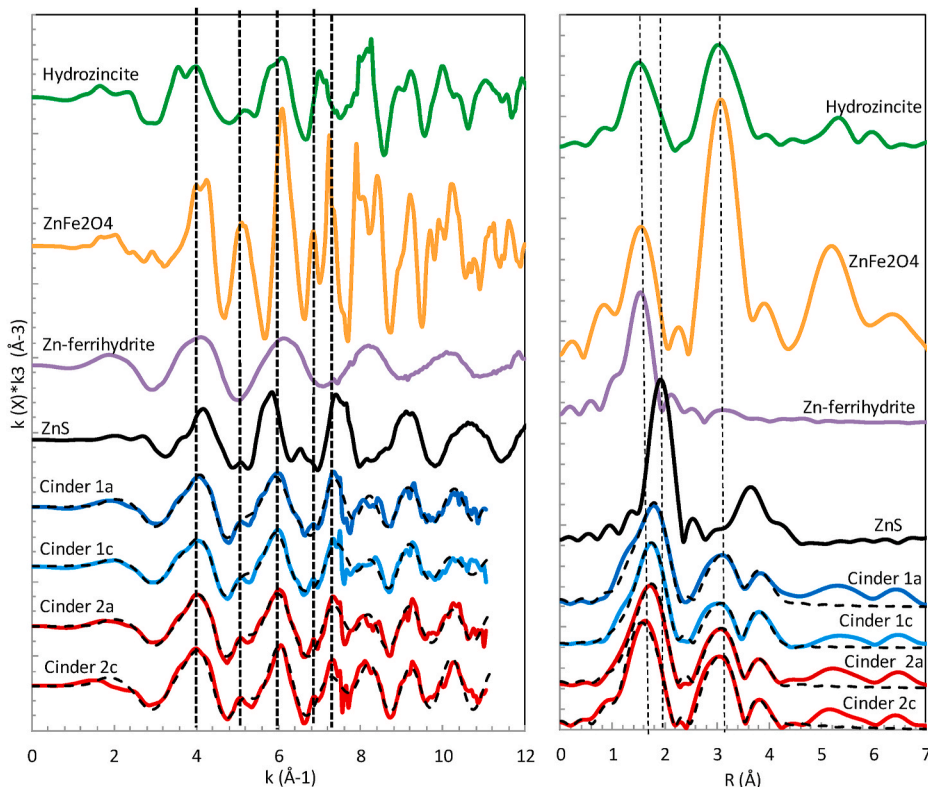
Fig. 4. a) Stacked k^3-weighted K-edge EXAFS spectra for Zn. Solid lines are measured spectra and dashed lines are model fits (shell fitting). b) Fourier transforms (FT magnitudes) of the k^3-weighted EXAFS spectra. [Print in color].

Table 5
Summary of EXAFS fits for Zn.

Sample	Path	CN	R (Å)	σ^2 (Å^2)	ΔE (eV)	S_0^2
Cinder 1a	Zn–O	1.81 (0.77)	1.99 (0.06)	0.006	0.53 (0.57)	0.7
	Zn–S	2.36 (0.76)	2.33 (0.03)	0.006		
	Zn⋯Fe	4	3.51 (0.03)	0.007 (0.002)		
	Zn⋯Zn	4	3.77 (0.20)	0.018 (0.020)		
	Zn⋯S2	4	4.41 (0.05)	0.007 (0.005)		
	Zn–O⋯O	5.43 (0.20)	3.47	0.012	*k*-range used: 2.5–10 Å	
	Zn–S⋯S	7.08 (0.72)	4.21	0.012	R-factor (%): 2.2	
Cinder 1c	Zn–O	1.64 (0.43)	1.99 (0.04)	0.006	−1.62 (0.47)	0.7
	Zn–S	2.36 (0.40)	2.31 (0.02)	0.006		
	Zn⋯Fe	4	3.50 (0.04)	0.009 (0.002)		
	Zn⋯Zn	4	3.77 (0.12)	0.016 (0.020)		
	Zn⋯S2	4	4.34 (0.03)	0.007 (0.006)		
	Zn–O⋯O	4.91 (0.18)	3.40	0.012	*k*-range used: 2.5–10 Å	
	Zn–S⋯S	7.08 (0.59)	4.19	0.012	R-factor (%): 1.5	
Cinders 2a	Zn–O	2.21 (0.51)	2.00 (0.02)	0.006	1.12 (0.37)	0.7
	Zn–S	1.99 (0.51)	2.33 (0.04)	0.006		
	Zn⋯Fe	4	3.51 (0.02)	0.006 (0.001)		
	Zn⋯Zn	4	3.72 (0.11)	0.015 (0.007)		
	Zn⋯S2	4	4.41 (0.04)	0.009 (0.005)		
	Zn–O⋯O	6.63 (0.10)	3.37	0.012	*k*-range used: 2.5–10 Å	
	Zn–S⋯S	5.97 (0.51)	4.22	0.012	R-factor (%): 0.8	
Cinders 2c	Zn–O	3.46 (0.67)	2.00 (0.04)	0.006	0.32 (0.38)	0.7
	Zn–S	1.38 (0.80)	2.34 (0.05)	0.006		
	Zn⋯Fe	4	3.51 (0.02)	0.003 (0.001)		
	Zn⋯Zn	4	3.70 (0.08)	0.011 (0.005)		
	Zn⋯S2	4	4.44 (0.06)	0.012 (0.007)		
	Zn–O⋯O	10.38 (0.13)	3.40	0.012	*k*-range used: 2.5–10 Å	
	Zn–S⋯S	4.14 (0.60)	4.16	0.012	R-factor (%): 1.2	

[a] CN = Coordination number; R = Atomic distance; σ^2 = Debye-Waller factor; ΔE = Energy shift parameter; S_0^2 = Passive amplitude reduction factor; *R-factor* = goodness-of-fit parameter of the Fourier Transform; sum of the squares of the differences between the data and the fit at each data point, divided by the sum of the squares of the data at each corresponding point. In general, R-factor values less than 5% are considered to reflect a reasonable fit. Uncertainties of fitted parameters as given in Artemis (Ravel and Newville, 2005).

was supersaturated in some samples. Jarosite was found to be undersaturated (See supplementary material, Table S3).

3.4. Speciation of Zn

3.4.1. Zn EXAFS

The cinder Zn spectra for the samples (cinder 1a, 1c, 2a, 2c) are very similar, which indicate an alike Zn speciation (Fig. 4). The displayed

spectra are from samples ground in a ball mill. It was concluded that the ball mill grinding did not affect the speciation of the sample by comparing with spectra from samples homogenized with a mortar. Visual comparison of Zn EXAFS cinder spectra with the reference spectra in Fig. 4 indicates that several Zn species are present in the cinder. No single reference spectrum matches the cinder spectra within the whole spectral range. However, the cinder spectra have obvious features from $ZnFe_2O_4$ (franklinite) and ZnS (sphalerite), see Fig. 4. Franklinite is an oxide mineral formed by high temperature metamorphism (Roberts et al., 2002; Zhang et al., 2011) while ZnS is an ore mineral.

More detailed information on Zn coordination in the pyrite cinders was obtained by development of model spectra (Table 5). Both Zn–O and Zn–S paths were identified in the first shell, indicating that some Zn is bound to both oxygen and sulfur. Both the path lengths of the first shell, Zn–O of about 2.0 Å and Zn–S of about 2.3 Å and the multiple scattering paths (Zn–O⋯O and Zn–S⋯S) are consistent with tetrahedral coordination. Zn has a octahedral coordination to O in solution (Trivedi et al., 2001) but tetrahedral coordination in $ZnFe_2O_4$ (Steenari and Norén, 2008) as well as to S in Zn sulfide minerals (Karlsson and Skyllberg, 2007; Steenari and Norén, 2008). Tetrahedrally coordinated Zn is also present in several other minerals, e.g. zincite, hydrozincite, hemimorphite (Medas et al., 2014); and adsorbs to iron hydroxides (Trivedi et al., 2001; Waychunas et al., 2002). With a mainly tetrahedral coordination to O and S, the fitting parameters for the first shell indicate that about half of Zn is bound to S and half to O.

The WT transform analysis shows that the intensity of the WT modulus is enhanced at about k 7–8 Å^{-1} and R+ΔR 3–4 Å (white/brown areas in Fig. 5 a-d). This indicates presence of a heavy backscatterer like Fe and/or Zn at 3.5–4.5 Å from Zn. Higher shells were fit with Zn⋯Fe at about 3.5 Å, Zn⋯Zn at about 3.7 Å and Zn⋯S at about 4.4 Å (Table 5). The distances are consistent with $ZnFe_2O_4$ and ZnS (Steenari and Norén, 2008). In other minerals, the second shell Zn⋯Zn or Zn⋯Fe distance is often about 3.2–3.3 Å, e.g. zincite, hydrozincite, hemimorphite (Medas et al., 2014), although for Zn inner sphere sorption to iron hydroxide, distances varying between 3.1 and 3.5 have been identified depending on the iron (hydr)oxide and pH (Cismasu et al., 2013; Waychunas et al., 2002). The WT of model spectra (shell fitted) for the pyrite cinder samples correspond very well with the sample spectra (Fig. 5).

In the LCF analysis, good fits were obtained with the three standards ZnS, franklinite ($ZnFe_2O_4$) and Zn-ferrihydrite (Zn-fh) (Table 6) as well as with the same three reference spectra plus hydrozincite ($Zn_5(CO_3)_2(OH)_6$) (not shown) while the other references did not contribute to the LCF. Addition of hydrozincite only affected the calculated amount of Zn-ferrihydrite, which was reduced to about half the value given in Table 6. Franklinite and ZnS remained essentially the same. In summary, the LCF results indicate that about 40–50% of the Zn is bound in ZnS, about 10–20% in franklinite, and about 30–40% in other forms, probably including adsorption to iron (hydr)oxides and hydrozincite but possibly also other species. These results are essentially consistent with the shell-fitting analysis. The proportion of ZnS is the same but shell fitting analysis suggests more franklinite and less of "other Zn forms" than the LCF analysis. The uncertainties given in Table 6 are statistical uncertainties calculated in Athena. The "actual" uncertainties are larger. The uncertainty of a similar system was estimated to about 10% (Isaure et al., 2002). In accordance, it may be assumed that constituents containing less than 10% of the measured element may not be identified (Strawn and Baker, 2008).

The EDTA extractable fraction of Zn, 29%–48% (Tiberg et al., 2017) matches fairly well with the fraction Zn-fh in the LCF analysis (Table 6), indicating that EDTA dissolves most of the Zn *not* associated to ZnS or $ZnFe_2O_4$ phases.

3.4.2. SEM-EDS analysis of the grain cross section

Fig. 6 shows a cross-section of a grain with a grey shell of hematite and iron (hydr)oxides and a light grey colored unreacted core that is composed of S, Zn and Fe. The unreacted core can be assumed to be
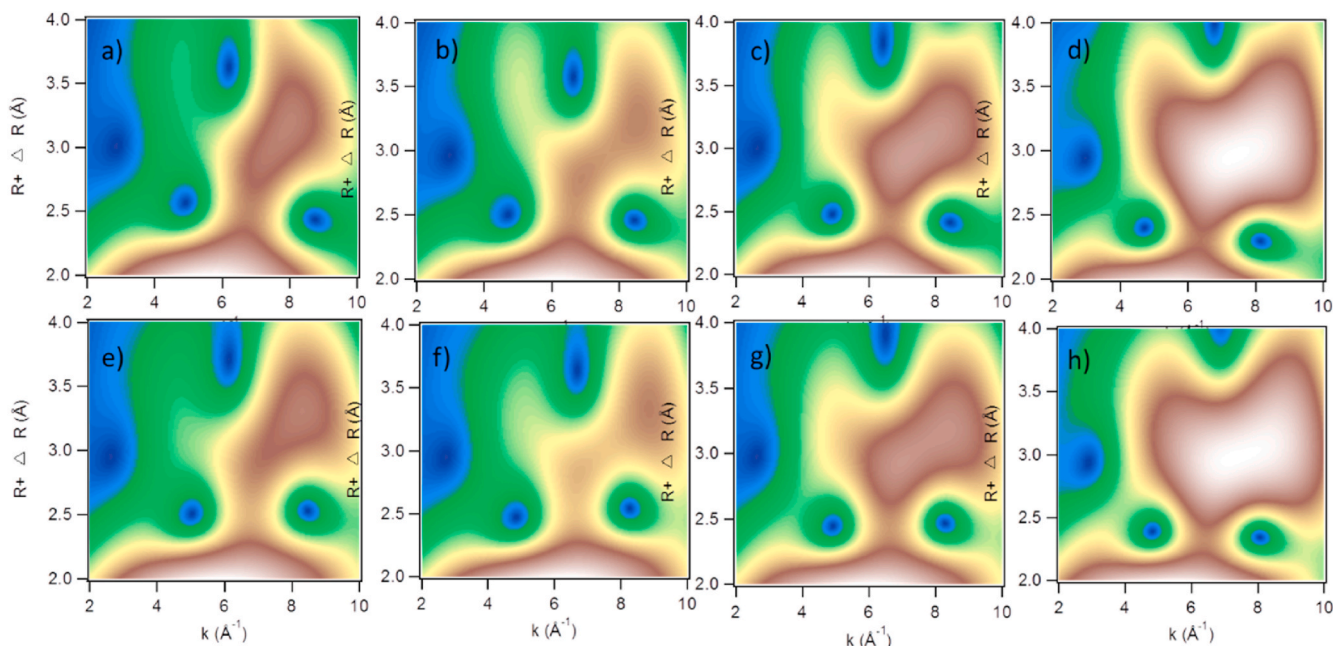
Fig. 5. Wavelet transforms of EXAFS spectra and models from measurements at the zinc k-edge. a) Spectrum Cinder 1a, b) Spectrum Cinder 1c, c) Spectrum Cinder 2a, d) Spectrum Cinder 2c, e) Model Cinder 1a, f) Model Cinder 1c, g) Model Cinder 2a, h) Model Cinder 2c. [Print in color].

Table 6
Linear combination fitting of Zn EXAFS spectra, weight uncertainty within brackets.

	$ZnFe_2O_4$ (%)[a]	ZnS (%)[a]	Zn-fh (%)[a]	r-value[b] (%)
Cinder 1a	16 (4)	53 (3)	31 (3)	11.3
Cinder 1c	14 (2)	52 (3)	34 (5)	17.0
Cinder 2a	19 (1)	47 (4)	34 (3)	11.5
Cinder 2c	21 (5)	30 (3)	49 (4)	15.3

[a] Statistical uncertainty of the LCF analysis calculated by Athena (Ravel and Newville, 2005).

[b] The R factor is the goodness-of-fit parameter reported by Athena software and calculated as the sum ((data-fit)^2)/sum (data^2) (Ravel and Newville, 2005).

sphalerite, as also have been identified by X-ray diffraction, EXAFS and supported by the XANES analysis.

EDS-spectra of some grain shells also showed the presence of Zn in combination with O and Fe, indicating franklinite, which was identified in the EXAFS-analysis. The findings are supported by (Balarini et al., 2008 and references therein) who reported incomplete grain roasting of sphalerite, and the forming of $ZnFe_2O_4$ in the process, as major obstacles in hydrometallurgical extraction of Zn from sulfide ores.

Zinc was also found on grain surfaces in combination with oxygen and without iron. This indicates the presence of zinc oxides such as zincite (ZnO) or Zn(OH)$_2$. According to the calculated saturation indexes (Table S3) these minerals are undersaturated at eigen pH in the cinder but geochemical modelling (Tiberg et al., 2017) shows that both minerals may form at slightly higher pH or Zn concentrations. The EXAFS analysis could not detect zincite (ZnO) nor Zn(OH)$_2$. In summary, ZnO and Zn(OH)$_2$ may be present but not at high concentrations (<10%).

3.5. Speciation of Pb

3.5.1. SEM-EDS analysis of precipitates at the surface and inclusions in the grain interior

At the surfaces on most of the grains, white/light grey spots where identified as Pb-bearing precipitates (Fig. 1). The EDS-spectra of the precipitate denoted *3* in Fig. 1 showed mainly Fe, O, S, Pb and small amounts of As (Fig. 7).

Fig. 8 show two examples (*A* and *B*) of cross-sections of grains with a porous matrix of iron (hydr)oxides with inclusions in light grey. The EDS-spectrum and the analytical interpretation software indicated that the inclusion in light grey is composed of Pb and O. A sulfur peak at 2.309 keV was not identified, but the existence of a hidden sulfur peak cannot be excluded (Newbury and Ritchie, 2014).

Previous studies have reported that the presence of sulfur favors the formation of condensed sulfate phases, such as anglesite, on grain surfaces (Díaz-Somoano et al., 2006; Folgueras et al., 2003; Miller et al., 2002; Yang et al., 2009). However, some experimental studies of sulfur rich systems (Folgueras et al., 2003; Galbreath et al., 2000; Oliveira et al., 2012) report not only the formation of anglesite, but also PbO and PbO·SiO$_2$ preferentially at smaller particle sizes, <10 nm (Oliveira et al., 2012).

The results confirm that Pb has escaped the sulfide minerals as vapour during the roasting process, condensed and formed precipitates on the external and interior surfaces of the porous iron (hydr)oxide grains that was formed. The elemental composition of the precipitate at the surface indicates anglesite. This conclusion is also supported by the calculation of saturation indexes, which indicated close to saturation with respect to anglesite at eigen pH (Table S3). The analytical interpretation of the elemental composition of the inclusions in the interior of the grains indicates PbO. But as PbMα and SKα are candidates for peak misidentification, anglesite is also possible.

3.6. Environmental risk

The high total concentrations of Zn and Pb in the cinder together with unreacted sulfide ore minerals constitute a potential for environmental impact. The sulfide ore and minerals formed in the roasting process, such as franklinite and anglesite, exhibit low solubility at neutral pH conditions and the mobility of Zn and Pb is governed by sorption on Fe oxides/hydroxides. Depending on the buffering capacity and reaction rates, oxidation of remaining sulfide residues and the release of protons might increase the metal leaching from the pyrite cinder. However the risk of acid drainage in the Bergvik cinder deposit seems to be minor since the residual sulfide has been identified as
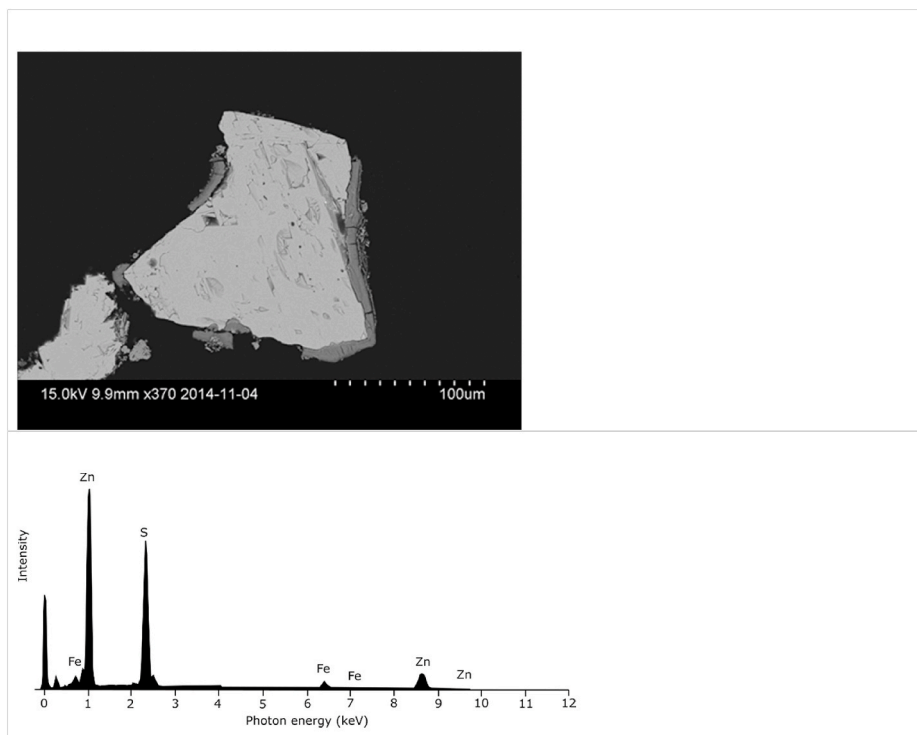
Fig. 6. SEM image of a cross-section of a grain with a grey shell of hematite and iron (hydr)oxides and the light grey colored unreacted core. The EDS-spectrum show that the unreacted core is composed of S, Zn and Fe, which indicates sphalerite.
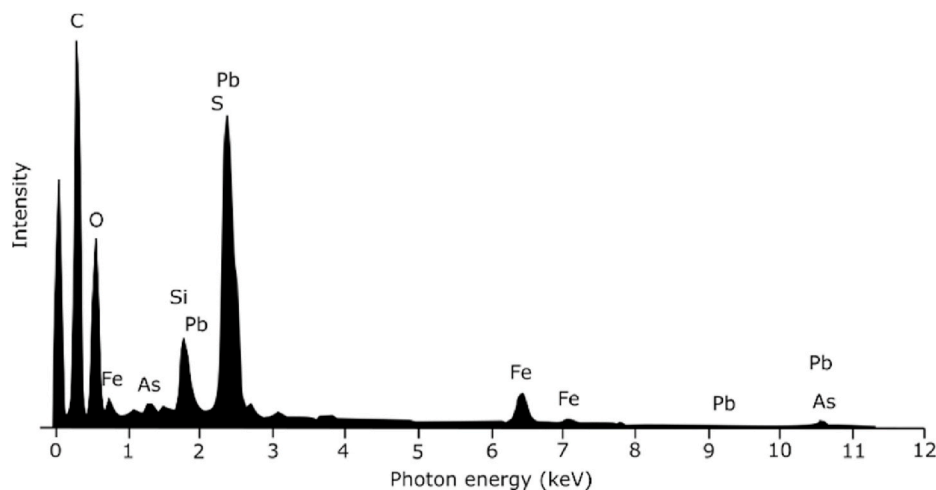
Fig. 7. The EDS-spectra of the precipitate previously shown in Fig. 1 (denoted 3 in image B). shows S, Pb, O and Fe, and small amounts of As. Here the main sulfur peak at 2.309 keV partly overlap the Pb-peak at 2.342 keV.

predominately sphalerite, the pH of the cinder is almost neutral and since the reaction kinetics was proven to be slow (Tiberg et al., 2017). Remediation strategies should focus on limiting exposure to atmosphere in order to minimize the risk that acid drainage develop with time.
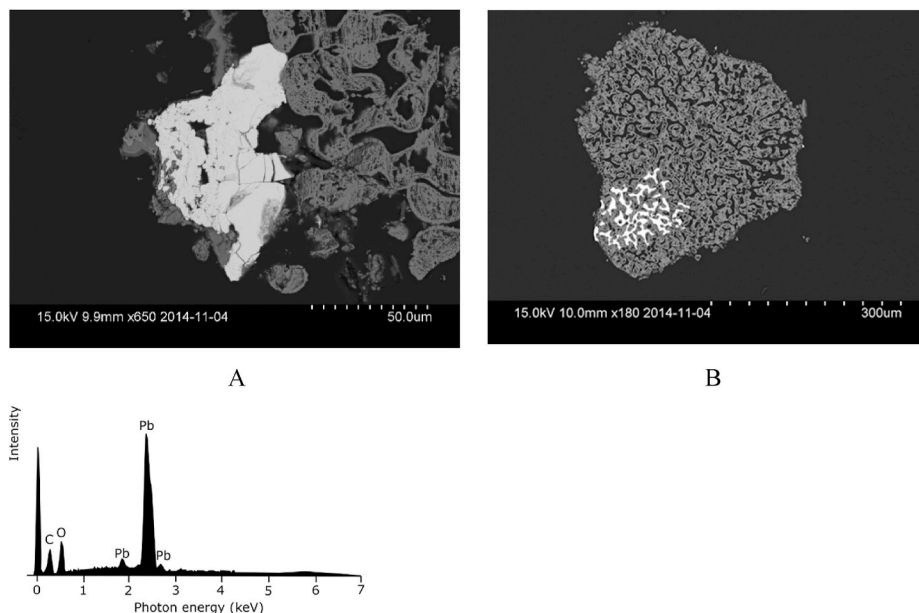
4. Conclusions

- Scanning electron microscopy with EDS showed pyrite cinder grains consisting mainly of a core of sulfide ore mineral, enclosed in layers of mainly hematite and iron hydr (oxides).
- Bulk element analysis showed that the residual sulfur in the cinder is 55–80% sulfide. The detection of sphalerite by EXAFS spectroscopy, X-ray diffraction analysis and SEM-EDS shows that sulfur is predominately associated with sphalerite. Sphalerite is not considered

to be an acid producing mineral, and this may be one explanation of the unusually high eigen pH (6.5–7.1). The remaining mass of sulfur is assumed to be adsorbed and/or precipitated as secondary sulfate minerals, predominantly associated with the grain surfaces. Calculated saturation indexes (SI) for a range of minerals indicate anglesite, aluminite and barite as possible sulfate secondary minerals.
- EXAFS spectroscopy showed that about half of Zn is directly associated with S and half with O. LCF analysis indicated sphalerite (40–50%), franklinite (10–20%), and the remaining mass as Zn-ferrihydrite and possibly hydrozincite. Zinc was also found on grain surfaces together with oxygen. Calculated saturation indexes indicated hydrozincite ($Zn_5(CO_3)_2(OH)_6$), but ZnO and $Zn(OH)_2$ cannot be excluded. Sphalerite is present in the original ore while the identified franklinite ($ZnFe_2O_4$) was likely formed during roasting

Fig. 8. SEM images of cross-sections of grains with a porous matrix of iron (hydr)oxides (grey) and inclusions of a condensed Pb phase (light grey in the figure). The EDS spectrum of the inclusion in the SEM image A shows Pb and O.

and other Zn species (including minerals and complexes on iron (hydr)oxide surfaces) may have formed during cooling and storing in the deposit.

- Previous work indicates that adsorption to Fe (hydr)oxides is an important retention mechanism for Pb in pyrite cinder (Tiberg et al., 2017). Here, SEM-EDS analysis showed precipitates of Pb minerals both on the surface of the grains and in the interior as inclusions. The mineral precipitates at the surfaces where composed of Pb, O, and S, indicating anglesite. The EDS analysis of the inclusions showed Pb and O, indicating PbO or possible anglesite since the existence of a hidden sulfur peak could not be excluded. The calculated saturation indexes indicated close to saturation with respect to anglesite at eigen pH of the cinder. The precipitates have likely been formed in the roasting process where Pb has escaped the sulfide minerals and condensed on external or interior surfaces of the porous grains.
- The study has confirmed the importance and added value of using a combination of complementary techniques to analyze the solid phase.

Declaration of competing interest

The authors declare that they have no known competing financial interests or personal relationships that could have appeared to influence the work reported in this paper.

Appendix A. Supplementary data

Supplementary data to this article can be found online at https://doi.org/10.1016/j.apgeochem.2021.105010.

References

Almkvist, G., Boye, K., Persson, I., 2010. K-edge XANES analysis of sulfur compounds: an investigation of the relative intensities using internal calibration. J. Synchrotron Radiat. https://doi.org/10.1107/S0909049510022946.

Balarini, J.C., Polli, L. de O., Miranda, T.L.S., Castro, R.M.Z. de, Salum, A., 2008. Importance of roasted sulphide concentrates characterization in the hydrometallurgical extraction of zinc. Miner. Eng. https://doi.org/10.1016/j.mineng.2007.10.002.

Bigham, J.M., Nordstrom, D.K., 2000. Iron and aluminum hydroxysulfates from acid sulfate waters. Rev. Mineral. Geochem. 40, 351–403. https://doi.org/10.2138/rmg.2000.40.7.

Caruccio, F.T., 1968. An evaluation of factors affecting acid mine drainage production and the ground water interaction in selected areas of Western Pennsylvania. In: Second Symposium Coal Mine Drainage Research, pp. 107–151. Pittsburgh.

Chukalina, M., 2010. Wavelet2.ipf, a procedure for calculating the Wavelet transform in IGOR Pro. http://www.esrf.eu/UsersAndScience/Experiments/CRG/BM20/Software/Wavelets/IGOR.

Cismasu, A.C., Levard, C., Michel, F.M., Brown, G.E., 2013. Properties of impurity-bearing ferrihydrite II: insights into the surface structure and composition of pure, Al- and Si-bearing ferrihydrite from Zn(II) sorption experiments and Zn K-edge X-ray absorption spectroscopy. Geochem. Cosmochim. Acta. https://doi.org/10.1016/j.gca.2013.05.040.

Curtin, D., Syers, J.K., 1990. Extractability and adsorption of sulphate in soils. J. Soil Sci. https://doi.org/10.1111/j.1365-2389.1990.tb00065.x.

Debret, B., Andreani, M., Delacour, A., Rouméjon, S., Trcera, N., Williams, H., 2017. Assessing sulfur redox state and distribution in abyssal serpentinites using XANES spectroscopy. Earth Planet Sci. Lett. 466 https://doi.org/10.1016/j.epsl.2017.02.029.

Díaz-Somoano, M., Unterberger, S., Hein, K.R.G., 2006. Prediction of trace element volatility during co-combustion processes. Fuel. https://doi.org/10.1016/j.fuel.2005.10.013.

Dold, B., National Environmental Engineering Research Institute, I, 2010. Basic concepts in environmental geochemistry of sulfidic mine-waste management. In: Sunil, Kumar (Ed.), Waste Management. IntechOpen Limited, London, UK, London. https://doi.org/10.5772/8458.

Eneroth, E., Bender Koch, C., 2003. Crystallite size of haematite from thermal oxidation of pyrite and marcasite - effects of grain size and iron disulphide polymorph. In: Minerals Engineering, pp. 1257–1267. https://doi.org/10.1016/j.mineng.2003.07.004.

ESRF, 2019. Sulfur reference spectra [WWW Document]. Beamline ID21, Database Inorg. sulfur Compd. URL. https://www.esrf.fr/home/UsersAndScience/Experiments/XNP/ID21/php/Database-SCompounds.html.

Folgueras, M.B., Díaz, R.M., Xiberta, J., Prieto, I., 2003. Volatilisation of trace elements for coal-sewage sludge blends during their combustion. In: Fuel. https://doi.org/10.1016/S0016-2361(03)00152-2.

Funke, H., Scheinost, A.C., Chukalina, M., 2005. Wavelet analysis of extended x-ray absorption fine structure data. Phys. Rev. B 71, 94110.

Galbreath, K.C., Toman, D.L., Zygarlicke, C.J., Pavlish, J.H., 2000. Trace element partitioning and transformations during combustion of bituminous and subbituminous U. S. Coals in a 7-kW combustion system. Energy Fuels 14, 1265–1279. https://doi.org/10.1021/ef000105n.

Garrels, R.M., Thompson, M.E., 1960. Oxidation of pyrite by iron sulfate solutions. Am. J. Sci. 258, 57–67.

Guadalix, M.E., Pardo, M.T., 1991. Sulphate sorption by variable charge soils. J. Soil Sci. https://doi.org/10.1111/j.1365-2389.1991.tb00107.x.

Heidel, C., Tichomirowa, M., Breitkopf, C., 2011. Sphalerite oxidation pathways detected by oxygen and sulfur isotope studies. Appl. Geochem. https://doi.org/10.1016/j.apgeochem.2011.08.007.

Hu, G., Dam-Johansen, K., Wedel, S., Hansen, J.P., 2006. Decomposition and oxidation of pyrite. Prog. Energy Combust. Sci. https://doi.org/10.1016/j.pecs.2005.11.004.

Isaure, M.P., Laboudigue, A., Manceau, A., Sarret, G., Tiffreau, C., Trocellier, P., Lamble, G., Hazemann, J.L., Chateigner, D., 2002. Quantitative Zn speciation in a contaminated dredged sediment by μ-PIXE, μ-SXRF, EXAFS spectroscopy and principal component analysis. Geochem. Cosmochim. Acta. https://doi.org/10.1016/S0016-7037(01)00875-4.

Jambor, J., 2003. Mine-waste mineralogy and mineralogical perspectives of acid-base accounting. In: Jambor, J., Blowes, D., Ritchie, A.I. (Eds.), Environmental Aspects of Mine Wastes. Mineralogical association of Canada, Vancouver, British Columbia, Canada, pp. 117–145.

Karlsson, T., Skyllberg, U., 2007. Complexation of zinc in organic soils - EXAFS evidence for sulfur associations. Environ. Sci. Technol. https://doi.org/10.1021/es0608803.

Lapakko, K., 2002. MMSD working paper No. 67 metal mine rock and waste characterization tools: an overview. https://pubs.iied.org/g00559.

Lin, Z., Qvarfort, U., 1996. Predicting the mobility of Zn, Fe, Cu, Pb, Cd from roasted sulfide (pyrite) residues - a case study of wastes from the sulfuric acid industry in Sweden. Waste Manag. 16, 671–681. https://doi.org/10.1016/S0956-053X(97)00009-3.

Liu, C., Huang, Y., Wang, X., Zhang, S., Xia, W., Sun, C., Liu, H., 2017. Dynamic experimental investigation on the volatilization behavior of lead and cadmium in the simulated municipal solid waste (MSW) influenced by sulfur compounds during incineration. Energy Fuels. https://doi.org/10.1021/acs.energyfuels.6b01315.

McKibben, M.A., Barnes, H.L., 1986. Oxidation of pyrite in low temperature acidic solutions: rate laws and surface textures. Geochem. Cosmochim. Acta 50, 1509–1520. https://doi.org/10.1016/0016-7037(86)90325-X.

Medas, D., Lattanzi, P., Podda, F., Meneghini, C., Trapananti, A., Sprocati, A., Casu, M.A., Musu, E., De Giudici, G., 2014. The amorphous Zn biomineralization at Naracauli stream, Sardinia: electron microscopy and X-ray absorption spectroscopy. Environ. Sci. Pollut. Res. https://doi.org/10.1007/s11356-013-1886-4.

Miller, B.B., Dugwell, D.R., Kandiyoti, R., 2002. Partitioning of trace elements during the combustion of coal and biomass in a suspension-firing reactor. Fuel 81, 159–171. https://doi.org/10.1016/S0016-2361(01)00134-X.

Miot, J., Lu, S., Morin, G., Adra, A., Benzerara, K., Küsel, K., 2016. Iron mineralogy across the oxycline of a lignite mine lake. Chem. Geol. https://doi.org/10.1016/j.chemgeo.2016.04.013.

Moncur, M.C., Jambor, J.L., Ptacek, C.J., Blowes, D.W., 2009. Mine drainage from the weathering of sulfide minerals and magnetite. Appl. Geochem. https://doi.org/10.1016/j.apgeochem.2009.09.013.

Newbury, D.E., Ritchie, N.W.M., 2014. Performing elemental microanalysis with high accuracy and high precision by scanning electron microscopy/silicon drift detector energy-dispersive X-ray spectrometry (SEM/SDD-EDS). J. Mater. Sci. https://doi.org/10.1007/s10853-014-8685-2.

Nordström, D.K., 1982. Aqueous pyrite oxidation and the consequent formation of secondary iron minerals. In: Hossner, L.R., J, A.K., D, F.F. (Eds.), Acid Sulfate Weathering: Pedogeochemistry and Relationship to Manipulation of Soil Materials. Soil Science Society of American Press, Madison.

Oliveira, M.L.S., Ward, C.R., Izquierdo, M., Sampaio, C.H., de Brum, I.A.S., Kautzmann, R.M., Sabedot, S., Querol, X., Silva, L.F.O., 2012. Chemical composition and minerals in pyrite ash of an abandoned sulphuric acid production plant. Sci. Total Environ. 430, 34–47. https://doi.org/10.1016/j.scitotenv.2012.04.046.

Peacock, C.L., Sherman, D.M., 2004. Copper(II) sorption onto goethite, hematite and lepidocrocite: a surface complexation model based on ab initio molecular geometries and EXAFS spectroscopy. Geochem. Cosmochim. Acta 68. https://doi.org/10.1016/j.gca.2003.11.030.

Pérez-López, R., Sáez, R., Álvarez-Valero, A.M., Nieto, J.M., Pace, G., 2009. Combination of sequential chemical extraction and modelling of dam-break wave propagation to aid assessment of risk related to the possible collapse of a roasted sulphide tailings dam. Sci. Total Environ. 407, 5761–5771. https://doi.org/10.1016/j.scitotenv.2009.07.031.

Persson, I., Lyczko, K., Lundberg, D., Eriksson, L., Pjaczek, A., 2011. Coordination chemistry study of hydrated and solvated lead(II) ions in solution and solid state. Inorg. Chem. https://doi.org/10.1021/ic1017714.

Ravel, B., Newville, M., 2005. ATHENA, artemis, hephaestus: data analysis for X-ray absorption spectroscopy using IFEFFIT. J. Synchrotron Radiat. 12, 537–541. https://doi.org/10.1107/S0909049505012719.

Roberts, D.R., Scheinost, A.C., Sparks, D.L., 2002. Zinc speciation in a smelter-contaminated soil profile using bulk and microspectroscopic techniques. Environ. Sci. Technol. 36, 1742–1750. https://doi.org/10.1021/es015516c.

Sahuquillo, A., Rigol, A., Rauret, G., 2003. Overview of the use of leaching/extraction tests for risk assessment of trace metals in contaminated soils and sediments. TrAC Trends Anal. Chem. (Reference Ed.). https://doi.org/10.1016/S0165-9936(03)00303-0.

Sánchez España, J., López Pamo, E., Santofimia Pastor, E., Reyes Andrés, J., Martín Rubí, J.A., 2006. The removal of dissolved metals by hydroxysulphate precipitates during oxidation and neutralization of acid mine waters, Iberian Pyrite Belt. Aquat. Geochem. https://doi.org/10.1007/s10498-005-6246-7.

Sandell, J.F., Dewey, G.R., Sutter, L.L., Willemin, J.A., 1996. Evaluation of lead-bearing phases in municipal waste combustor fly ash. J. Environ. Eng. (34), 34–40. https://doi.org/10.1061/(ASCE)0733-9372(1996)122:1.

Sandström, M., Jalilehvand, F., Damian, E., Fors, Y., Gelius, U., Jones, M., Salomé, M., 2005. Sulfur accumulation in the timbers of King Henry VIII's warship Mary Rose: a pathway in the sulfur cycle of conservation concern. Proc. Natl. Acad. Sci. U.S.A. 102, 14165–14170. https://doi.org/10.1073/pnas.0504490102.

Savage, K.S., Tingle, T.N., O'Day, P.A., Waychunas, G.A., Bird, D.K., 2000. Arsenic speciation in pyrite and secondary weathering phases, mother lode gold district, tuolumne county, California. Appl. Geochem. https://doi.org/10.1016/S0883-2927(99)00115-8.

Schwertmann, U., Cornell, R.M., 2000. Iron Oxides in the Laboratory: Preparation and Characterization. Wiley, Weinheim.

Singer, P.C., Stumm, W., 1970. Acidic mine drainage: the rate-determining step. Science 167, 1121–1123. https://doi.org/10.1126/science.167.3921.1121.

Spadini, L., Manceau, A., Schindler, P.W., Charlet, L., 1994. Structure and stability of Cd2+ surface complexes on ferric oxides. 1. Results from EXAFS spectroscopy. J. Colloid Interface Sci. 168 https://doi.org/10.1006/jcis.1994.1395.

Steenari, B.-M., Norén, K., 2008. Zinks förekomstformer i aska studerade med en röntgenabsorptionsspektrometrisk metod, Miljöriktig användning av askor.

Strawn, D.G., Baker, L.L., 2008. Speciation of Cu in a contaminated agricultural soil measured by XAFS, μ-XAFS, and μ-XRF. Environ. Sci. Technol. 42 https://doi.org/10.1021/es071605z.

The Essential Chemical Industry, the Essential Chemical Industry - Online [WWW Document], n.d. . Univ. York.

Tiberg, C., Bendz, D., Theorin, G., Kleja, D.B., 2017. Evaluating solubility of Zn, Pb, Cu and Cd in pyrite cinder using leaching tests and geochemical modelling. Appl. Geochem. 85 https://doi.org/10.1016/j.apgeochem.2017.09.007.

Trivedi, P., Axe, L., Tyson, T.a., 2001. An analysis of zinc sorption to amorphous versus crystalline iron oxides using XAS. J. Colloid Interface Sci. 244, 230–238. https://doi.org/10.1006/jcis.2001.7971.

Trivedi, P., Dyer, J.A., Sparks, D.L., 2003. Lead sorption onto ferrihydrite. 1. A macroscopic and spectroscopic assessment. Environ. Sci. Technol. 37 https://doi.org/10.1021/es0257927.

Vamerali, T., Bandiera, M., Coletto, L., Zanetti, F., Dickinson, N.M., Mosca, G., 2009. Phytoremediation trials on metal- and arsenic-contaminated pyrite wastes (Torviscosa, Italy). Environ. Pollut. 157, 887–894. https://doi.org/10.1016/j.envpol.2008.11.003.

Waychunas, G.A., Fuller, C.C., Davis, J.A., 2002. Surface complexation and precipitate geometry for aqueous Zn(II) sorption on ferrihydrite I: X-ray absorption extended fine structure spectroscopy analysis. Geochem. Cosmochim. Acta. https://doi.org/10.1016/S0016-7037(01)00853-5.

Williamson, M.A., Rimstidt, J.D., 1994. The kinetics and electrochemical rate-determining step of aqueous pyrite oxidation. Geochem. Cosmochim. Acta. https://doi.org/10.1016/0016-7037(94)90241-0.

Yang, C., Chen, Y., Peng, P., Li, C., Chang, X., Wu, Y., 2009. Trace element transformations and partitioning during the roasting of pyrite ores in the sulfuric acid industry. J. Hazard Mater. 167, 835–845. https://doi.org/10.1016/j.jhazmat.2009.01.067.

Zabinsky, S.I., Rehr, J.J., Ankudinov, A., Albers, R.C., Eller, M.J., 1995. Multiple-scattering calculations of x-ray-absorption spectra. Phys. Rev. B 52, 2995–3009.

Zhang, Y., Yu, X., Li, X., 2011. Zinc recovery from franklinite by sulphation roasting. Hydrometallurgy. https://doi.org/10.1016/j.hydromet.2011.07.002.